

Nonlinear multimodal interference and saturable absorption using a short graded-index multimode optical fiber

Elham Nazemosadat,¹ and Arash Mafi^{1,*}

¹*Department of Electrical Engineering and Computer Science,
University of Wisconsin-Milwaukee, Milwaukee, WI 53211, USA*

**Corresponding author: mafi@uwm.edu*

Compiled September 13, 2018

A detailed investigation of the nonlinear multimodal interference in a short graded-index multimode optical fiber is presented. The analysis is performed for a specific device geometry, where the light is coupled in and out of the multimode fiber via single-mode fibers. The same device geometry was recently used to obtain ultra-low-loss coupling between two single-mode optical fibers with very different mode-field diameters. Our results indicate the potential application of this simple geometry for nonlinear devices, such as in nonlinear switching, optical signal processing, or as saturable absorbers in mode-locked fiber lasers. Saturable absorption in this all-fiber configuration is discussed and it is shown that it provides attractive properties that can potentially be used in high pulse energy mode-locked fiber lasers. © 2018 Optical Society of America

OCIS codes: 060.2310 (Fiber optics); 190.4370 (Nonlinear optics, fibers); 060.7140 (Ultrafast processes in fibers); Non-linear optics in multimode fibers.

1. Introduction

Multimode interference (MMI) in optical fibers has been used successfully in recent years for various device applications including, beam shapers, sensors, and filters [1–8]. MMI in a graded-index multimode optical fiber (GIMF) was recently used to create very low-loss couplers between two single mode optical fibers (SMFs) with very different mode-field diameters [9,10]. Here, the linear analysis of Ref. [9] is extended and the MMI effect in the nonlinear regime for the GIMF-coupler geometry shown in Fig. 1 is investigated. The main intention of this study is to explore the possibility of using the simple SMF-GIMF-SMF geometry in nonlinear device applications, such as in optical signal processing [11] or as a saturable absorber (SA) in mode-locked fiber lasers [12,13].

GIMFs are commonly used in fiber-optic communications to reduce modal dispersion, as the group velocities of all modes are nearly identical at the design wavelength [14,15]. However, GIMFs exhibit another unique property that makes them very attractive for MMI applications: the propagation constants of their modes are equally spaced. Consequently, their self-imaging lengths can be very short, even less than 1 mm [9]; therefore, it is possible to make extremely short (even submillimeter) practical MMI devices [10] or easily tune the length of the GIMF coupler for a specific MMI application [10].

In this paper, our studies are focused on the simplest case of nonlinear MMI (NL-MMI) in the setup shown in Fig. 1 with identical input and output SMFs; this choice is also the most practical one for most device applications. Our results will elucidate some general behaviors of such couplers in the nonlinear regime. More complex geometries involving different fiber junctions and using various mode conversion techniques [16] such as long-

period gratings [17] can modify some of the observations and conclusions; however, such complex modifications are less likely to be adopted in practical device applications in the near future. We hope that our results can be a useful starting point for future studies of NL-MMI and mode conversion in more complex systems.

NL-MMI has been studied in various contexts over the years (see, for example, Ref. [18]). Generally speaking, nonlinear devices that operate based on nonlinear mode switching and coupling in spatially separated waveguides can also be viewed as MMI devices [19–22]. Nonlinear polarization rotation is another important example of NL-MMI (between two orthogonal polarization modes) that closely resembles our analysis here [23,24].

In Section 2, a general overview of GIMFs, nonlinear propagation in multimode optical fibers, and MMI are presented. NL-MMI in GIMFs in the context of the SMF-GIMF-SMF geometry of Fig. 1 is discussed in Section 3. In Subsection A, a reduced version of the model which includes only two propagating modes is analyzed; this simplification helps us to develop proper insight into the physics of NL-MMI in GIMFs. In Subsection B, our analysis is extended to the realistic case of five propagating modes; the impact of the presence of additional propagating modes in the NL-MMI setup can be shown by comparing these results with the results of Subsection A. In Section 4, the saturable absorption behavior of the SMF-GIMF-SMF geometry is analyzed as an example of the utility of this setup for device applications. The concluding remarks are presented in Section 5, where it is shown that the SMF-GIMF-SMF geometry can be a viable design for nonlinear switching or saturable absorption.

The formalism and results in this paper are mainly laid out in dimensionless units; this choice is common in

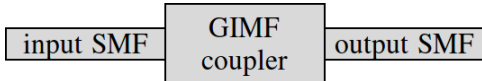


Fig. 1. A GIMF of length L is used as an intermediate coupler between two SMF fibers. In Refs. [9,10], this geometry was used to create very low-loss couplers between two SMFs with very different mode-field diameters. In this paper, nonlinear MMI effects for identical input and output SMFs are explored.

nonlinear fiber optics, because it reduces the number of parameters and prevents redundancy in the analysis. For real-world applications, it is easy to convert back to the dimensionful parameters; in Section 5, the performance of a NL-MMI SA device with specific parameters from commercially available optical fibers is analyzed.

In order to reduce the complexity of the analysis and to make the problem more tractable, the studies in this paper are considered in the continuous wave (CW) limit. In practice, after the design parameters are chosen based on the CW analysis, the temporal effects can be included to optimize the final design. GIMFs, if used near their optimal design wavelengths, are particularly attractive for short-pulse ultrafast applications compared with other MMFs. The low modal dispersion in GIMFs ensures that pulses do not break up in short GIMF segments [25], making the CW analysis an adequate approximation.

Finally, it should be pointed out that the transmission through the SMF-GIMF-SMF geometry is a periodic function of the frequency of the light source [9,10]. For mode-locking applications where short pulses are generated with very large spectral bandwidth, the length of the GIMF needs to be sufficiently short to provide the necessary spectral transmission window. Moreover, the SMF-GIMF-SMF geometry can be potentially used as the spectral filter that is required to stabilize the mode-locking operation of normal-dispersion high-energy femtosecond fiber lasers [26].

2. Fundamentals

In the following three subsections, a brief general overview of GIMFs (Subsection A), nonlinear multimode propagation of light in GIMFs (Subsection B), and the general formulation of the MMI phenomenon in GIMFs in the context of the SMF-GIMF-SMF coupler (Subsection C) will be presented. The formulation presented in this section will be used to analyze the nonlinear behavior of the SMF-GIMF-SMF geometry in detail in subsequent sections.

A. Overview of GIMFs

The refractive index profile of a GIMF is given by

$$n^2(\rho) = n_0^2 \left[1 - 2\Delta \left(\frac{\rho}{R} \right)^\alpha \right], \quad (1)$$

where R is the core radius, n_0 is the refractive index at the center of the core, Δ is the index step, $\alpha \approx 2$ characterizes a near parabolic-index profile in the core ($\rho \leq R$), and $\alpha = 0$ in the cladding ($\rho > R$). The transverse electric field profile of a confined mode, with radial p ($p \geq 0$) and angular m integer numbers, can be expressed as [25]

$$E_{p,m}(\rho, \phi) = N_p^m \frac{\rho^{|m|}}{\rho_0^{|m|+1}} \exp\left(-\frac{\rho^2}{2\rho_0^2}\right) L_p^{|m|}\left(\frac{\rho^2}{\rho_0^2}\right) e^{im\phi}, \quad (2)$$

where $L_p^{|m|}$ are generalized Laguerre polynomials, and ρ_0 and N_p^m are given by

$$\rho_0 = \frac{R^{1/2}}{(k_0 n_0)^{1/2} (2\Delta)^{1/4}}, \quad N_p^m = \sqrt{\frac{p!}{\pi(p+|m|)!}}, \quad (3)$$

where $k_0 = 2\pi/\lambda$. The coefficients N_p^m of these Laguerre-Gauss modes (LG_{pm}) are chosen such that the modes are orthonormal. Using the bra-ket notation, the electric field profile of the LG_{pm} mode is identified as $|p, m\rangle = E_{p,m}(\rho, \phi)$ and the orthonormality condition is expressed as $\langle p, m | p', m' \rangle = \delta_{p,p'} \delta_{m,m'}$, where the bra-ket indicates integration in the transverse (ρ - ϕ) coordinates.

All modes with equal group mode number $g = 2p + |m| + 1$ are almost degenerate in the value of the propagation constant, which is given according to the formula

$$\beta_{(g)} = n_0 k (1 - 2\Delta X_g)^{1/2}, \quad (4)$$

where

$$X_g = \left(\frac{g}{\sqrt{N_\alpha}} \right)^{2\alpha/(\alpha+2)}. \quad (5)$$

N_α is the total number of guided modes (counting the polarization degeneracy) and is given by

$$N_\alpha = \frac{\alpha}{\alpha+2} n_0^2 k_0^2 R^2 \Delta. \quad (6)$$

While the analysis presented in this article is generally applicable to a wide range of GIMFs and is presented in dimensionless units, for specific numerical arguments and comparisons, the parameters of a conventional high-bandwidth commercial-grade GIMF such as Corning's InfiniCor[®] eSX+ will be used; this fiber is optimized for high bandwidth performance at 850 nm wavelength, with the core radius of $R = 25 \mu\text{m}$. The specified GIMF will be referred to as C-GIMF standing for the *conventional GIMF*. It should be noted that the key spatial dimension in a GIMF that sets all its modal properties is not the core radius R , but is $\rho_c = \sqrt{2}\rho_0$, where ρ_0 is defined in Eq. 3. ρ_c is the mode radius of the LG₀₀ mode; for C-GIMF, $\rho_c \approx 7.7 \mu\text{m}$ at 1550 nm wavelength and $\rho_c \approx 5.7 \mu\text{m}$ at 850 nm wavelength.

B. Overview of nonlinear propagation in GIMFs

Consider an input optical field injected into the core of the GIMF. The injected field excites the LG_{pm} modes of the GIMF with different amplitudes $A_{p,m}(0)$; $A_{p,m}(z)$ will be regarded as the envelope of the electric field and $z = 0$ indicates the input end of the GIMF [25]. In order to simplify our notation, the collective index μ will be used to represent the p, m index pair of the LG_{pm} modes; i.e., $\mu \equiv (p, m)$ in the rest of this section. However, when necessary, we will directly use the (p, m) labels or specify how to translate the μ index into the (p, m) index pair. $|A_\mu(z)|^2$ represents the optical power in the LG_{pm} mode.

In the scalar approximation, the generalized nonlinear Schrödinger equation (GNLSE) describing the CW longitudinal evolution of $A_{p,m}(z)$ can be written as

$$\frac{\partial A_\mu}{\partial z} = i\delta\beta_\mu A_\mu + i\gamma \sum_{\nu, \kappa, \xi} \tilde{\eta}_{\mu\nu\kappa\xi} A_\nu A_\kappa A_\xi^*. \quad (7)$$

where $\delta\beta_\mu = \beta_\mu - \beta_{(1)}$, β_μ is the propagation constant of the mode with the collective index μ and $\beta_{(1)}$ is the propagation constant of the LG₀₀ mode with $g = 1$ from Eq. 4. The “normalized” nonlinear coupling coefficient is a fully symmetric tensor and is defined as $\tilde{\eta}_{\mu\nu\kappa\xi} = \gamma_{\mu\nu\kappa\xi}/\gamma$ where

$$\gamma_{\mu\nu\kappa\xi} = \left(\frac{n_2\omega_0}{c}\right) \int d^2x E_\mu^* E_\nu E_\kappa E_\xi^*. \quad (8)$$

In Eq. 8, E_μ is the shorthand notation for $E_{p,m}(\rho, \phi)$. $\gamma = \gamma_{0000}$ is the nonlinear coefficient of the LG₀₀ mode, n_2 is the nonlinear index coefficient, and ω_0 is the carrier frequency. For the lowest order mode LG₀₀ for which ρ_c is simply the modal radius, one can define $\gamma_{0000} = n_2\omega_0/A_{\text{eff}}^0$, where $A_{\text{eff}}^0 = \pi\rho_c^2$. The total optical power in the GIMF is given by $\tilde{P} = \sum_\mu |A_\mu(z)|^2$ and is conserved in propagation along the GIMF; i.e., $\partial_z \tilde{P} = 0$.

It is more convenient to express the GNLSE in dimensionless units. B_μ can be defined as

$$B_\mu(z) = \frac{1}{\sqrt{\tilde{P}}} A_\mu(z) e^{-i\gamma\tilde{P}z}, \quad (9)$$

and rescale the longitudinal coordinate z by the difference between the propagation constants of the first and the second mode groups $\beta_{(1)} - \beta_{(2)}$,

$$\zeta = z \times (\beta_{(1)} - \beta_{(2)}). \quad (10)$$

Using these transformations, Eq. 7 can be simplified as

$$\partial_\zeta B_\mu = -i(r_\mu + \tilde{\gamma})B_\mu + i\tilde{\gamma} \sum_{\nu, \kappa, \xi} \tilde{\eta}_{\mu\nu\kappa\xi} B_\nu B_\kappa B_\xi^*, \quad (11)$$

where Eq. 11 is expressed in terms of the dimensionless coefficients

$$r_\mu = \frac{\beta_\mu - \beta_{(1)}}{\beta_{(2)} - \beta_{(1)}}, \quad \tilde{\gamma} = \frac{\gamma\tilde{P}}{\beta_{(1)} - \beta_{(2)}}. \quad (12)$$

and can be solved for the dimensionless field B_μ in terms of the dimensionless longitudinal coordinate ζ . It can be realized that the rescaled fields B_μ satisfy the power conservation condition $\sum_\mu |B_\mu(z)|^2 = 1$ at any points along the GIMF.

Using Eq. 4, Eq. 5, and the fact that $X_g \ll 1$, one can show that r_μ is non-negative and is nearly an integer: $r_\mu \approx g_\mu - 1$, where g_μ is the group number associated with mode μ [10].

C. Overview of MMI in GIMFs

The particular setup that is considered in this paper is shown in Fig. 1 and consists of injecting a nearly Gaussian beam from the input SMF, which is spliced to the input facet of the GIMF, and collecting the light at the other end of the GIMF from the output SMF. If the normalized mode of the input SMF is defined as $|\text{in}\rangle$, where $\langle \text{in} | \text{in} \rangle = 1$, the mode amplitude in the GIMF at the input can be written as $A_\mu(0) = \sqrt{\tilde{P}} \langle p, m | \text{in} \rangle$, where $|p, m\rangle$ is the GIMF mode defined in Eq. 2.

The relative transmitted power to the output SMF is given by

$$\tau = \frac{1}{\tilde{P}} |\langle \text{out} | E(\rho, \phi, L) \rangle|^2, \quad (13)$$

where $|\text{out}\rangle$ is the normalized mode of the output SMF, and $|E(\rho, \phi, L)\rangle$ is the total field at the output facet of the GIMF with a length of L , calculated from

$$E(\rho, \phi, L) = e^{i\beta_{(1)}L} \sum_\mu A_\mu(L) E_\mu(\rho, \phi). \quad (14)$$

Identical input and output SMFs are the focus of this paper ($|\text{in}\rangle \equiv |\text{out}\rangle$), for which the relative power transmission can be written as

$$\tau = \frac{1}{\tilde{P}^2} \left| \sum_\mu A_\mu^*(0) A_\mu(z) \right|^2 = \left| \sum_\mu B_\mu^*(0) B_\mu(z) \right|^2. \quad (15)$$

The injected beam from the input SMF is in the form of a Gaussian with radius w and can be expressed as

$$|\text{in}\rangle = \sqrt{\frac{2}{\pi w^2}} \exp\left(-\frac{\rho^2}{w^2}\right). \quad (16)$$

Because of the azimuthal symmetry of the input Gaussian beam, if the input SMF is centrally aligned with the GIMF, only LG_{p0} ($m = 0$) modes can be excited in the GIMF. The excitation amplitude can be calculated as [9]

$$B_p(0) = \frac{2\sqrt{\eta}}{\eta + 1} \Psi^p, \quad \eta = \frac{\rho_c^2}{w^2}, \quad \Psi = \frac{\eta - 1}{\eta + 1}. \quad (17)$$

In Fig. 2, the excitation amplitudes of the LG_{p0} modes are displayed as a function of the radial number p , for three different values of the η parameter. For the case of $\eta = 1$ (not shown in Fig. 2), only the LG₀₀ mode is excited, because the input Gaussian beam is mode-matched to the LG₀₀ mode of the GIMF. For a slightly larger value of $\eta = 1.1$, only 0.2% of power is coupled to

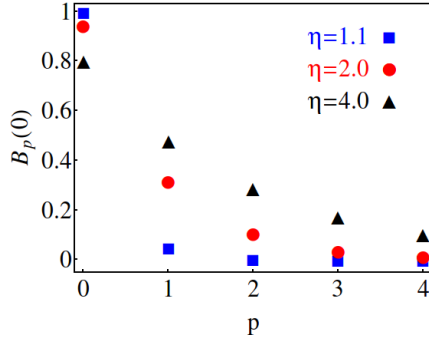


Fig. 2. The excitation amplitudes of the LG_{p0} modes from Eq. 17 are plotted as a function of the radial number p , for three different values of the η parameter.

the LG_{01} mode and the power coupled to higher order modes is negligible. For the larger value of $\eta = 4$, only 64% of the power is coupled to the LG_{00} mode. In this case, the relative power coupled to the LG_{01} , LG_{02} , and LG_{03} modes are 23%, 8%, and 3%, respectively. $\eta = 4$ is obtained when coupling the C-GIMF to an SMF with the mode-field diameter of nearly $7.7 \mu\text{m}$ at 1550 nm wavelength. For coupling of the C-GIMF to Corning[®] SMF-28TM (SMF-28) with the mode-field diameter of $10.4 \mu\text{m}$ at 1550 nm wavelength, the value of η is nearly equal to 2.2.

There are two reasons for not exploring the case of $\eta < 1$ in this manuscript. First, under the $\eta \rightarrow \eta^{-1}$ transformation, Eq. 17 remains unchanged except for an overall multiplicative factor of $(-1)^p$ [9]. Despite this change in the the initial phase, no new insight is obtained in overall observations and general conclusions presented in this paper. Second, η is larger than unity for most combinations of commercially available SMFs and GIMFs. Therefore, our analysis are limited to $\eta > 1$ to avoid adding unnecessary complexity.

3. NL-MMI: SMF-GIMF-SMF geometry

In the following, our studies will only include the case of $m = 0$ or zero-angular momentum modes (see the discussion in Subsection C). The experimental evidence presented in Refs. [9, 10] confirms the reliability of this choice. Moreover, using the formalism outlined in Ref. [25], it can be shown that the conservation of angular momentum, dictated by the symmetries of the nonlinear coupling terms, prevents the excitation of any modes with $m \neq 0$ along the fiber from only $m = 0$ modes; therefore, our analysis can be safely limited to the small and manageable zero-angular momentum subset of modes. It is worth mentioning that $m \neq 0$ modes may still be excited because of the bending and imperfections in the fiber; this issue will be addressed in Section 5 but for now, our analysis are limited to the subspace of $m = 0$ modes.

Because only LG_{p0} modes are considered in the analysis, one can readily identify the collective index μ used

in Section 2 with the radial mode number p .

Therefore, all the indexes in the relevant equations such as in Eqs. 7, 8, 11, and 14 can be directly replaced with the radial mode numbers of the LG_{p0} modes.

In a typical GIMF, only a handful of $m = 0$ modes are supported in the core; for example, only five $m = 0$ modes are supported at 1550 nm wavelength in a C-GIMF. Even for such a small number of modes, the GNLSE will have many terms and becomes quite complicated. In order to develop the proper fundamental understanding and intuition on the key mechanisms involved in the NL-MMI of these modes in a GIMF, our analysis are initially limited to the smaller subset of LG_{00} and LG_{10} modes in Subsection A. This way, the physics of the NL-MMI in the SMF-GIMF-SMF is not buried under the complexity introduced by the large number of modes propagating in the GIMF. Eventually, in Subsection B, the number of propagating modes in the GIMF will be increased to five, considering LG_{00} through LG_{40} , and the similarities and differences between the two-mode and the five-mode scenarios will be explored.

As a reference for comparison with nonlinear couplings for self-phase modulation and cross-phase modulation in conventional SMFs [24], the nonlinear coupling terms among the three lowest order modes in GIMFs; i.e., LG_{00} , LG_{10} , and LG_{20} , are: $\tilde{\eta}_{0001} = \tilde{\eta}_{0011} = \tilde{\eta}_{1111} = 1/2$, $\tilde{\eta}_{0012} = \tilde{\eta}_{0022} = 3/8$, $\tilde{\eta}_{2222} = 11/32$, $\tilde{\eta}_{1122} = 5/16$, $\tilde{\eta}_{0002} = \tilde{\eta}_{0111} = \tilde{\eta}_{0112} = \tilde{\eta}_{1112} = 1/4$, $\tilde{\eta}_{0122} = 3/16$, $\tilde{\eta}_{1222} = 11/64$, $\tilde{\eta}_{0222} = 5/32$.

A. NL-MMI with LG_{00} and LG_{10} modes

In this subsection, it is assumed that only LG_{00} and LG_{10} modes are excited in the GIMF and the optical power is distributed only between these two modes. It should be taken into account that this assumption is only strictly valid for $\eta \approx 1$ from Eq. 17 ($p_0 \gg p_1$ in that case). However, our intention in this section is not to simulate an exact experimentally realizable configuration in the spirit of Fig. 1; rather, this limited two-mode subspace is used to gain insight into the physics of NL-MMI in GIMFs. Therefore, in this subsection, the limitations of Eq. 17 are abandoned and it is assumed that $p_0 + p_1 = 1$, where $p_0 = |B_0|^2$ and $p_1 = |B_1|^2$ can adopt any (positive) values subject to this condition. In practice, it may be possible to create this scenario experimentally in a more complex setup than that of Fig. 1; e.g., by using mode conversion techniques; however, such details are beyond the scope and intentions of this subsection.

Using Eq. 11, the following coupled nonlinear equations are obtained:

$$\begin{aligned} \partial_\zeta B_0 &= i\tilde{\gamma}(|B_0|^2 + \frac{1}{4}|B_1|^2)B_0 + \frac{i\tilde{\gamma}}{2}(B_0^2 B_1^* + B_1^2 B_0^*), \\ \partial_\zeta B_1 &= -ir_1 B_1 + \frac{i\tilde{\gamma}}{2}B_0 \\ &+ \frac{i\tilde{\gamma}}{2}(-|B_1|^2 B_1 + B_0^2 B_1^* + \frac{1}{2}B_1^2 B_0^*), \end{aligned} \quad (18)$$

Nonlinear effects can be ignored when $\tilde{\gamma}\tilde{L} \approx 0$, where $\tilde{L} = L \times (\beta_{(1)} - \beta_{(2)})$ and L is the total length of the GIMF. In the absence of nonlinear effects, the solution to Eq. 18 can be written as

$$B_0(\zeta) = B_0(0), \quad B_1(\zeta) = e^{-ir_1\zeta}B_1(0). \quad (19)$$

In the linear case, the relative power of each mode is conserved; i.e., p_0 and p_1 remain unchanged along the GIMF. The relative power transmission in an SMF-GIMF-SMF setup in the linear limit with two modes can be calculated from Eq. 15 as

$$\tau = 1 - 4p_0p_1 \sin^2\left(\frac{r_1\tilde{L}}{2}\right). \quad (20)$$

The relative power transmission is a periodic function of the length of the GIMF and varies periodically between $\tau_{\min} = 1 - 4p_0p_1$ and $\tau_{\max} = 1$; $\tau_{\min} = 0$ in the special case where the power is equally distributed ($p_0 = p_1 = 1/2$). These issues have been discussed in further detail in Ref. [9], where the linear MMI in GIMFs is explored in the presence of multiple $m = 0$ modes.

The main parameters that determine the value of the relative power transmission in the SMF-GIMF-SMF setup are the relative power of the modes (p_0 and p_1), the normalized GIMF length (\tilde{L}), and the normalized nonlinear coefficient $\tilde{\gamma}$. In Fig. 3, the relative power transmission is plotted as a function of \tilde{L} for three different cases of $\tilde{\gamma} = 0$ (solid), $\tilde{\gamma} = 0.7$ (dashed), and $\tilde{\gamma} = 3$ (dotted); all cases are plotted for relative power values of $p_0 = p_1 = 0.5$. The linear case with $\tilde{\gamma} = 0$ clearly follows Eq. 20 where the oscillation periodicity of τ with respect to \tilde{L} (normalized GIMF length) is $T_L = 2\pi/r_1 \approx \pi$.

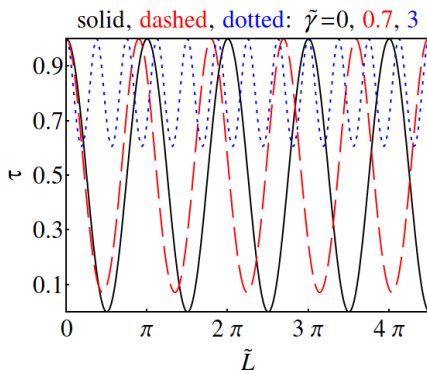


Fig. 3. The relative power transmission is plotted as a function of the normalized GIMF length \tilde{L} for the case of LG₀₀ and LG₁₀ modes when $p_0 = p_1 = 0.5$ at $\zeta = 0$, for $\tilde{\gamma} = 0$ (solid), $\tilde{\gamma} = 0.7$ (dashed), and $\tilde{\gamma} = 3$ (dotted).

When the nonlinear effects are small, the nonlinearity merely results in an additional phase mismatch between the LG₀₀ and LG₁₀ modes; e.g., for $\tilde{\gamma} = 0.7$, the accumulated nonlinear phase mismatch is nearly π at $\tilde{L} = 4.5\pi$ and is responsible for changing the $\tau = 0$ in the linear case to $\tau \approx 1$ for $\tilde{\gamma} = 0.7$ in Fig. 3. It should be emphasized that in the presence of nonlinearity, p_0 and p_1

are not conserved and vary periodically along the GIMF (LG₀₀ and LG₁₀ exchange power); however, unless we explicitly specify their ζ -dependence, when referring to p_0 and p_1 , we mean their initial value at the $\zeta = 0$ point in the GIMF and refrain from introducing new variables.

The linear and nonlinear cases of $\tilde{\gamma} = 0$ and $\tilde{\gamma} = 0.7$ differ in another important feature besides the cumulative nonlinear phase mismatch; the minimum value of τ for $\tilde{\gamma} = 0.7$ is larger than zero. This effect becomes more prominent for larger relative nonlinear coefficients. In fact, as can be seen for $\tilde{\gamma} = 3$ in Fig. 3, the relative power transmission remains above 60% for all values of \tilde{L} .

The relative power transmission explored in Fig. 3 is for the case of $p_0 = p_1 = 0.5$. In Fig. 4, similar situations as in Fig. 3 are considered, yet with $p_0 = 0.75$ and $p_1 = 0.25$ at $\zeta = 0$. The solid line relates to $\tilde{\gamma} = 0$ and follows Eq. 20. Similar to Fig. 3, the nonlinear phase mismatch between the LG₀₀ and LG₁₀ modes increases the frequency of oscillation of τ with respect of \tilde{L} as the relative nonlinear coefficient is increased. In the case of $\tilde{\gamma} = 3$ (dotted), the relative power transmission τ remains nearly equal to unity for all values of \tilde{L} . For large values of $\tilde{\gamma}$ (e.g. $\tilde{\gamma} = 3$), the power coupling between LG₀₀ and LG₁₀ modes is inefficient and the amplitude of the oscillation in the relative power carried by each mode as a function of \tilde{L} is small and is a decreasing function of $\tilde{\gamma}$. In other words, for a sufficiently large values of $\tilde{\gamma}$, p_0 and p_1 remain unchanged as they propagate through the GIMF. The cumulative phase of the LG₀₀ and LG₁₀ modes is also nearly identical for large $\tilde{\gamma}$ as the two modes propagate along the GIMF. The combined effects of the nearly unchanged relative power and the nearly identical cumulative phase of the modes results in the near unity value of τ in this situation.

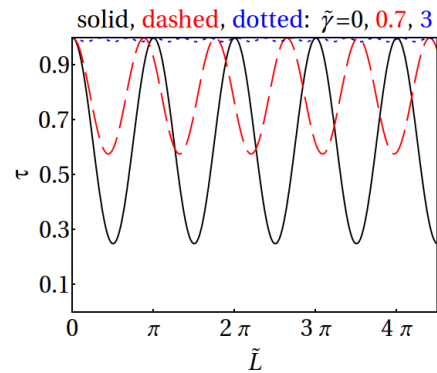


Fig. 4. Same as Fig. 3, except for $p_0 = 0.75$ and $p_1 = 0.25$ at $\zeta = 0$.

In Fig. 5, similar situations as in Fig. 4 are considered, yet with $p_0 = 0.25$ and $p_1 = 0.75$ at $\zeta = 0$. The solid line relates to $\tilde{\gamma} = 0$ and is identical to the case of $p_0 = 0.75$ and $p_1 = 0.25$ presented in Fig. 4, in agreement with Eq. 20. Similar to Fig. 4, increasing the relative nonlinear coefficient results in a larger oscillation frequency of τ with respect to \tilde{L} . However, in complete contrast to

the behavior observed in Fig. 4 for $\tilde{\gamma} \neq 0$, increasing $\tilde{\gamma}$ initially lowers the minimum value of τ and for sufficiently large value of $\tilde{\gamma}$, the minimum can even be equal to zero; if $\tilde{\gamma}$ is further increased, the minimum value of τ increases again and eventually settles asymptotically at a value that can be substantially different from zero. This behavior is dictated by a very efficient exchange of power between LG₀₀ and LG₁₀ modes as well as considerable difference between the cumulative phases of the modes; however, at a large $\tilde{\gamma}$ the cumulative phases of the modes become nearly identical.

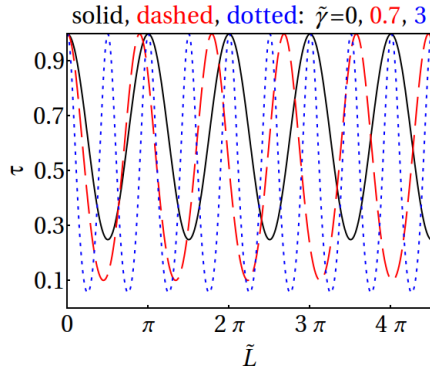


Fig. 5. Same as Fig. 3, except for $p_0 = 0.25$ and $p_1 = 0.75$ at $\zeta = 0$.

As discussed above, the dynamics of power coupling between the LG₀₀ and LG₁₀ modes is quite complex. In Fig. 6, $p_0(\zeta = \tilde{L})$ is plotted as a function of $p_0(\zeta = 0)$ for $\tilde{L} = 4.5\pi$. In the linear case, LG₀₀ and LG₁₀ modes are totally uncoupled and $p_0(\zeta = \tilde{L}) = p_0(\zeta = 0)$, as shown with the diagonal dashed line in Fig. 6. However, for $\tilde{\gamma} = 2$, nonlinearity couples the power between LG₀₀ and LG₁₀ modes and $p_0(\zeta = \tilde{L})$ oscillates as a function of $p_0(\zeta = 0)$, shown with the dotted line in Fig. 6. It can be seen that $p_0(\zeta = \tilde{L})$ oscillates more rapidly as $\tilde{\gamma}$ increases. In order to isolate the nonlinear effect, the dispersive term r_1 is set to zero and the power coupling curve for $\tilde{\gamma} = 2$ is re-plotted as the solid line in Fig. 6. Comparing the solid and dotted lines, it can be concluded that the effect of the dispersive term ($-ir_1B_1$) is to tame the oscillations, especially for p_0 near zero or unity.

For a longer GIMF (at fixed $\tilde{\gamma}$), the taming effect of the dispersive term will be even more pronounced and the amplitude of oscillations will be smaller. In Fig. 7, where \tilde{L} is assumed to be 50π , the “artificial” case of $r_1 = 0, \tilde{\gamma} = 0.5$ (dotted) oscillates rapidly and with large amplitude. However, for the real situation where $r_1 \approx 2$ (and $\tilde{\gamma} = 0.5$), the rapid oscillation is replaced with a smooth change (dashed line) that does not move far away from the diagonal virtual line of $p_0(\zeta = \tilde{L}) = p_0(\zeta = 0)$. Once the nonlinearity is increased to $\tilde{\gamma} = 1.0$, the oscillations reappear, yet with a much lower frequency and smaller amplitude (solid line) compared with the artificial case of $r_1 = 0$. It is noteworthy that the oscillations in the solid curve are mainly located in the region of the

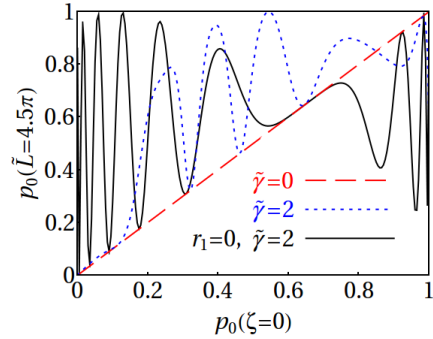


Fig. 6. This figure shows the exchange of power between the LG₀₀ and LG₁₀ modes, where p_0 at the output of the GIMF is plotted as a function of p_0 at the input for $\tilde{L} = 4.5\pi$.

graph where the dotted curve does not oscillate much.

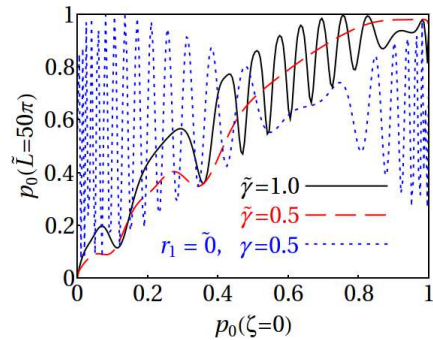


Fig. 7. Same as Fig. 6, except for $\tilde{L} = 50\pi$, and different choices of $\tilde{\gamma}$.

In order to examine the effect of the total power injected in the GIMF on the relative power transmission, the transmission is plotted as a function of $\tilde{\gamma}$ for the case of $\tilde{L} = 4.5\pi$ in Fig. 8. The length of the GIMF is chosen in such a way that for the linear case of $\tilde{\gamma} = 0$, relative power transmission τ is at its minimum value of $\tau_{\min} = 1 - 4p_0p_1$ for the three cases of $p_0 = 0.5, 0.25, 0.75$ shown in Fig. 8. In agreement with our previous discussions, increasing the power (increasing $\tilde{\gamma}$) results in an increase in the value of τ and the maximum transmission of $\tau_{\max} = 1$ is obtained for $\tilde{\gamma} \approx 0.65$, nearly independent of the initial value of p_0 . As $\tilde{\gamma}$ is further increased, τ decreases again and follows an oscillatory form as a function of $\tilde{\gamma}$.

In practical devices, the GIMF is often considerably longer than $(\beta_{(1)} - \beta_{(2)})^{-1}$; therefore, $\tilde{L} \gg 1$. In Fig. 9, a scenario identical to that explored in Fig. 8 is considered, except for a much longer GIMF with $\tilde{L} = 100.5\pi$. The main difference between the cases of $\tilde{L} = 100.5\pi$ in Fig. 9 and $\tilde{L} = 4.5\pi$ in Fig. 8 is that much lower power (much smaller $\tilde{\gamma}$) is required for the GIMF with $\tilde{L} = 100.5\pi$ to switch the relative power transmission from τ_{\min} to τ_{\max} ; for the case of $p_0 = 0.25$, the required $\tilde{\gamma}$ for power transmission switching is as low as ≈ 0.026 as can be seen in the dashed line in Fig. 9. Another im-

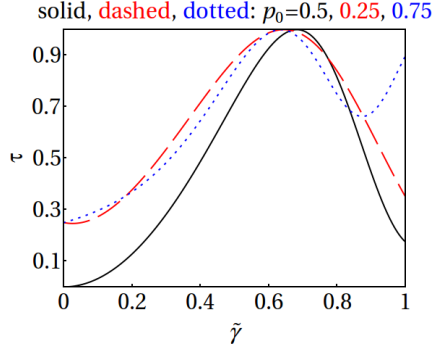


Fig. 8. The relative power transmission is plotted as a function of $\tilde{\gamma}$ (thus the total power) for $\tilde{L} = 4.5\pi$ for the case of LG_{00} and LG_{10} modes, when $p_0 = 0.5, 0.25, 0.75$ at $\zeta = 0$, in solid, dashed, and dotted lines, respectively.

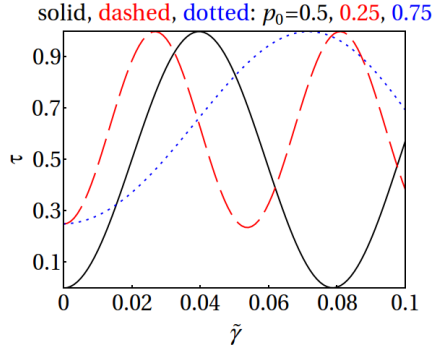


Fig. 9. Same as Fig. 8, except for $\tilde{L} = 100.5\pi$.

portant difference between the cases of $\tilde{L} = 4.5\pi$ and $\tilde{L} = 100.5\pi$ is that in the latter case, the value of $\tilde{\gamma}$ at which τ_{\max} is obtained is very sensitive to the initial distribution of the power among the modes.

B. Nonlinear MMI with LG_{00} through LG_{40} modes

In this subsection, the analysis of Subsection A is extended to the more realistic case of five propagating modes. As mentioned before, this is a realistic scenario for the case of a C-GIMF at 1550 nm wavelength. The general observations in this subsection and the similarities and differences with the two-mode scenario of Subsection A should cover the overall nonlinear dynamics in most realistic cases of NL-MMI in GIMFs.

In addition to the difference between the number of modes in this subsection versus Subsection A, here the initial excitation amplitudes are chosen such that they satisfy Eq. 17 (otherwise the problem would become intractable). The main advantage of this choice is that it complies with the configuration of Fig. 1 and can be tested experimentally. Another important difference is that in Subsection A, it was assumed that $p_0 + p_1 = 1$, which resulted in $\tau_{\max} = 1$. In a realistic case where Eq. 17 is applied and the number of guided modes is finite, some of the power coming from the input SMF is coupled to the radiation and cladding modes. Therefore, it can be shown (see Ref. [9]) that the maximum

transmission is given by

$$\tau_{\max} = (1 - \Psi^{2P})^2 \leq 1, \quad (21)$$

where Ψ is defined in Eq. 17 and P is the total number of propagating modes with $m = 0$: $P = 5$ in this subsection. Therefore, in all the plots shown in this subsection, $\tau_{\max} < 1$ and is given by Eq. 21.

In Fig. 10, the relative power transmission is plotted as a function of the normalized GIMF length \tilde{L} , for $\eta = 3 + \sqrt{8}$, which results in $p_0 = 0.5$. Similar to the two-mode scenario plotted in Fig. 3, the cases of $\tilde{\gamma} = 0$ (solid), $\tilde{\gamma} = 0.7$ (dashed), and $\tilde{\gamma} = 3$ (dotted) are analyzed. The linear case ($\tilde{\gamma} = 0$) in Fig. 10 is very similar to the two-mode case of Fig. 3, except that τ_{\min} and τ_{\max} are different due to the power leakage to the radiation and cladding modes, as explained above. However, the major difference is that at $\tilde{L} = 4.5\pi$, $\tilde{\gamma} = 0.7$ is not nearly enough to switch the relative power transmission from τ_{\min} (at $\tilde{\gamma} = 0$) to τ_{\max} in the five-mode scenario. In other words, higher power is required in the realistic five-mode scenario for transmission switching compared with the two-mode scenario. This is intuitively expected as the presence of the higher modes results in the distribution of the intensity over a larger cross-sectional area of the GIMF.

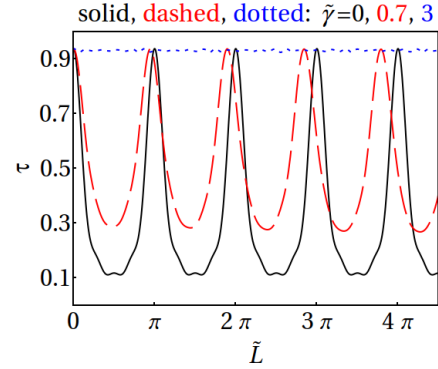


Fig. 10. The relative power transmission is plotted as a function of the normalized GIMF length \tilde{L} for the case of LG_{00} through LG_{40} modes (five zero angular modes) when $p_0 = 0.5$ at $\zeta = 0$ ($\eta = 3 + \sqrt{8}$), for $\tilde{\gamma} = 0$ (solid), $\tilde{\gamma} = 0.7$ (dashed), and $\tilde{\gamma} = 3$ (dotted). The results should be compared with Fig. 3 where only two modes LG_{00} and LG_{10} were considered.

Next, the case of $p_0 = 0.75$ for the five-mode scenario is considered in Fig. 11, which should be compared with the two-mode scenario in Fig. 4. According to Eq. 17, this case can be obtained by choosing $\eta = 3$. Unlike the case of $p_0 = 0.5$ studied above, there is a strong similarity between the five-mode and two-mode scenarios in the $p_0 = 0.75$ case; at $\tilde{L} = 4.5\pi$, $\tilde{\gamma} = 0.7$ is nearly sufficient to switch the relative power transmission from τ_{\min} (at $\tilde{\gamma} = 0$) to $\approx \tau_{\max}$. This result is quite important, because $\eta = 3$ is more readily achievable when using standard commercial fibers than such large values

as $\eta = 3 + \sqrt{8} \approx 5.8$. For example, as mentioned before, coupling C-GIMF to SMF-28 at 1550 nm, results in $\eta \approx 2.2$, or coupling 1060XP fiber from Thorlabs catalog to C-GIMF leads to $\eta \approx 4.27$ at 1060 nm wavelength. The major difference between the two-mode and five-mode scenarios is that at the higher value of $\tilde{\gamma} = 3$, τ experiences a much higher-amplitude oscillation as a function of \tilde{L} in the five-mode case. The large amplitude oscillations in the five-mode scenario for $\tilde{\gamma} = 3$ are due to the efficient power transfer from the lowest order mode to the other four modes; each mode accumulates a different linear and nonlinear phase as it propagates along the GIMF, resulting in large variations in the relative power transmission which is a sensitive function of both the amplitude and the phase of each mode (see Eq. 15).

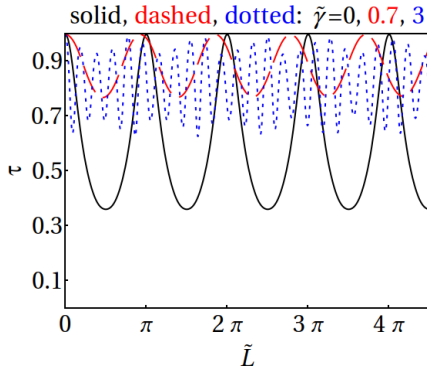


Fig. 11. Same as Fig. 10, except for $p_0 = 0.75$ at $\zeta = 0$ ($\eta = 3$). The results should be compared with Fig. 4 where only two modes LG_{00} and LG_{10} were considered.

Finally, the case of $p_0 = 0.25$ for the five-mode scenario is considered in Fig. 12, which should be compared with the two-mode scenario in Fig. 5. This case corresponds to $\eta = 7 + \sqrt{48} \approx 13.9$, which is very hard to obtain using conventional fibers. Substantial power leakage into the radiation and cladding modes is observed in the five-mode scenario and the results contrast sharply from the two-mode scenario in Fig. 5. Because of the finite number of core-guided modes supported by the finite GIMF core (see Eq. 6) which is truncated by the cladding at radius R , some of the power from the input SMF does not couple to the core-guided modes and couples to the cladding and radiation modes, as estimated in Eq. 21 and also discussed in Ref. [9]. The power leakage can be substantial for $\eta \gg 1$ as observed in Fig. 12. There is hardly any difference between the linear case ($\tilde{\gamma} = 0$) and $\tilde{\gamma} = 0.7$ in Fig. 12; however, for $\tilde{\gamma} = 3$, the relative power transmission nearly saturates over the entire value of \tilde{L} at τ_{\max} .

In summary, the NL-MMI related to $p_0 = 0.75$ in the five-mode scenario closely resembles that of the two-mode scenario presented in Subsection A. This similarity is lost as the value of p_0 is lowered (via increasing η); however, a larger value of p_0 is generally more accessible using commercially available optical fibers; fortunately, the power switching dynamics (from τ_{\min} to

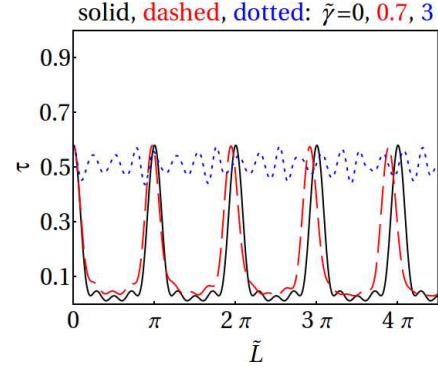


Fig. 12. Same as Fig. 10, except for $p_0 = 0.25$ at $\zeta = 0$ ($\eta = 7 + \sqrt{48}$). The results should be compared with Fig. 5 where only two modes LG_{00} and LG_{10} were considered.

τ_{\max}) is more desirable for $p_0 = 0.75$ than $p_0 = 0.25$ in the SMF-GIMF-SMF geometry shown in Fig. 1.

4. Saturable absorber using NL-MMI

In Section 3, the NL-MMI behavior of the SMF-GIMF-SMF geometry of Fig. 1 was discussed in great detail. Here, the results will be used to explore the application of this geometry as an SA. Specifically, it is desirable for the SMF-GIMF-SMF configuration to attenuate low power signals ($\tilde{\gamma} \approx 0$), but allow the higher power signals to go through. All analysis performed in this section is for the realistic case of five-modes (LG_{00} through LG_{40}), subject to the constraint of Eq. 17 for the initial excitation amplitudes.

Fig. 13 depicts the behavior of the relative power transmission τ as a function of $\tilde{\gamma}$ for a fixed value of $\tilde{L} = 4.5\pi$ in a SMF-GIMF-SMF configuration, for $p_0 = 0.5, 0.25, 0.75$ at $\zeta = 0$, in solid, dashed, and dotted lines. The value of \tilde{L} is chosen such that in the linear case, the relative power transmission is at its minimum value. In Subsection B, it was pointed out that the case of $p_0 = 0.75$ is the most interesting scenario from an experimental point of view. For $p_0 = 0.75$, the relative power transmission increases from τ_{\min} to $\tau_{\max} \approx 1$ monotonically as $\tilde{\gamma}$ is increased from zero to $\tilde{\gamma} \approx 0.75$. Beyond $\tilde{\gamma} \approx 0.75$, τ goes through a few low amplitude oscillations and saturates at $\tau_{\max} \approx 1$. This is nearly an ideal scenario for an SA, where the only downside with this design is that τ_{\min} is considerably larger than zero.

For $p_0 = 0.5$ in Fig. 13, a slightly higher value of $\tilde{\gamma}$ is required compared with $p_0 = 0.75$ to achieve the maximum transmission; moreover, more oscillations are observed beyond the transmission peak value, which may not be a desirable feature for an SA. Another important feature of this plot is the large low-transmission plateau and the sudden rise of τ near the peak values, which is desirable for pulse shortening in an SA. The case of $p_0 = 0.25$ is also shown in Fig. 13; the peak value of transmission in this scenario is only near 50% due to power coupling to the radiation and cladding modes, as

discussed in Subsection B, making this an undesirable design. The results in Fig. 13 should be compared with the two-mode scenario in Fig. 8. A notable feature in Fig. 8 is the large-amplitude oscillations of τ as a function of $\tilde{\gamma}$; this behavior is very different from Fig. 13 where τ was nearly saturated to τ_{\max} beyond $\tilde{\gamma} \approx 0.75$ for $p_0 = 0.75$.

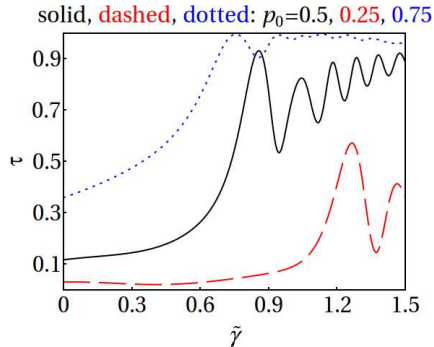


Fig. 13. The relative power transmission is plotted as a function of $\tilde{\gamma}$ (thus the total power) for $\tilde{L} = 4.5\pi$ for the case of five modes, when $p_0 = 0.5, 0.25, 0.75$ at $\zeta = 0$, in solid, dashed, and dotted lines, respectively.

In Fig. 14, a similar case to the one discussed in Fig. 13 is considered, except for a longer GIMF section where $\tilde{L} = 100.5\pi$. Similarly, this value of \tilde{L} is chosen such that in the linear case, the relative power transmission is at its minimum value. The most notable differences between the case of $\tilde{L} = 100.5\pi$ in Fig. 14 and $\tilde{L} = 4.5\pi$ in Fig. 13 are that τ_{\max} is obtained at a lower value of $\tilde{\gamma}$ for the longer GIMF design; this is somewhat expected, given that the nonlinear phase is cumulative. However, comparing the five-mode scenario in Fig. 14 with the two-mode case of Fig. 9, shows that much higher value of $\tilde{\gamma}$ is required in the five-mode scenario to obtain τ_{\max} ; therefore, the five-mode and two-mode scenarios differ substantially from each other.

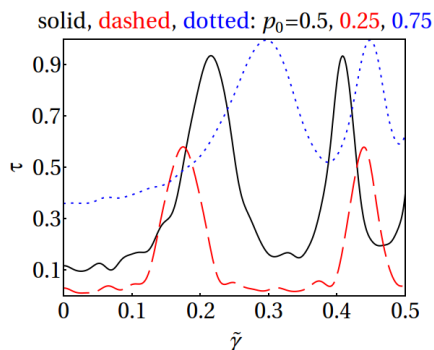


Fig. 14. Same as Fig. 13, except for $\tilde{L} = 100.5\pi$.

In Figs. 13 and 14, the value of \tilde{L} is chosen such that $\tau = \tau_{\min}$ is obtained for $\tilde{\gamma} = 0$. While this may seem a reasonable choice, however this is not required from an SA; rather, all that is required from an SA is to efficiently discriminate against low power signals with

minimal impact on the high power. Therefore, it is necessary to examine other possibilities for \tilde{L} and find the most efficient SA that is possible with the SMF-GIMF-SMF geometry of Fig. 1. A relevant metric for the pulse power discrimination in an SA is the value of $(\partial\tau/\partial\tilde{\gamma})$, which characterizes the sensitivity of an SA to a change in the pulse power.

Fig. 15 shows $(\delta\tau/\tau)$, defined as

$$(\delta\tau/\tau) = \frac{1}{\tau} \left(\tau|_{\tilde{\gamma}=0.001} - \tau|_{\tilde{\gamma}=0} \right), \quad (22)$$

as a function of the normalized GIMF length. $(\delta\tau/\tau)$ is used as the metric because it is related to $(\partial\tau/\partial\tilde{\gamma})$ via $(\delta\tau/\tau) \approx \tau^{-1}(\partial\tau/\partial\tilde{\gamma})\delta\tilde{\gamma}$ for $\delta\tilde{\gamma} = 0.001$. The normalized length of the GIMF is chosen to be $\tilde{L} = 300\pi + \delta\tilde{L}$, and the horizontal axis in Fig. 15 is expressed as $\delta\tilde{L}$ in the range $[-\pi/2, +\pi/2]$; the reason for this limited range in $\delta\tilde{L}$ is that $(\delta\tau/\tau)$ repeats in a nearly periodic fashion outside this range, unless $\delta\tilde{L}$ becomes very large. It will be discussed later in Section 5 that even a seemingly small value of $\tilde{\gamma} = 0.001$ can translate to multi-kilowatts of peak power in some commercial GIMFs, such as C-GIMF. Therefore, our main intention in choosing $\delta\tilde{\gamma} = 0.001$ in Eq. 22 and subsequent figures is to ensure that our design and observations are relevant for practical situations.

For both $\eta = 2$ (solid line) and $\eta = 3$ (dashed line) in Fig. 15, the maximum value of $(\delta\tau/\tau)$ is obtained at $\delta\tilde{L} \approx -0.4$, while the large low-transmission plateau already observed in Figs. 13 and 14 at near $\tilde{\gamma} = 0$ is responsible for the small value of $(\delta\tau/\tau)$ near $\delta\tilde{L} = 0$. The maximum value of $(\delta\tau/\tau)$ is around 1% for $\eta = 2$ and 5% for $\eta = 3$. It should be pointed out that SAs can be used to mode-lock lasers even when their modulation depth (MD) is as low as 0.5% [27]; MD is defined as the maximum change in transmission in an SA. Although MD is often the standard quantity used to assess the performance of SAs, the large values of MD obtained in the SMF-GIMF-SMF (between τ_{\min} and τ_{\max}) can be misleading, because a very high peak power may be needed to access the full range of the MD (some numerical values will be presented in Section 5). Therefore, $(\delta\tau/\tau)$ has been used in this paper, which is identical to MD within the reasonably accessible range of pulse peak powers.

It is required to ensure that the total transmission through the SMF-GIMF-SMF geometry is not too low; in other words, the SA is not too lossy near the peak value of $(\delta\tau/\tau)$. In Fig. 16, the average value $(\tau|_{\tilde{\gamma}=0.001} + \tau|_{\tilde{\gamma}=0})/2$ is plotted as a function of $\delta\tilde{L}$ for $\eta = 2$ (solid line) and $\eta = 3$ (dashed line). It can be seen that the average relative power transmission is reasonably large near the peak value of $(\delta\tau/\tau)$ of Fig. 15; therefore, the SA can be regarded as a viable design.

In Fig. 17, $(\delta\tau/\tau)$ is plotted in the same fashion as in Fig. 15, except for $\eta = 4$. The reason separate figures are used to plot $\eta = 2, 3$ and $\eta = 4$ is that the vertical scales are different. As can be seen in Fig. 17, $(\delta\tau/\tau)$ as large as

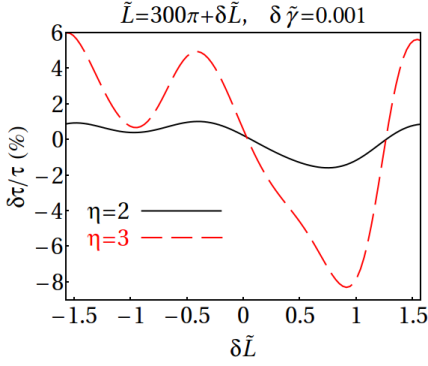


Fig. 15. The relative change in the normalized power transmission in the SMF-GIMF-SMF geometry defined in Eq. 22 plotted as a function of $\delta\tilde{L}$, where the length of the GIMF section is given by $\tilde{L} = 300\pi + \delta\tilde{L}$. A large positive value of $(\delta\tau/\tau)$ is desirable for saturable absorption. The plots are presented for $\eta = 2$ (solid) and $\eta = 3$ (dashed).

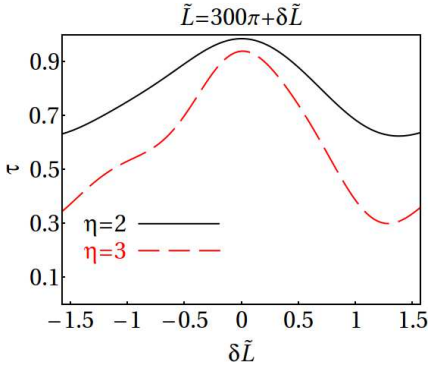


Fig. 16. The relative power transmission is shown as function of $\delta\tilde{L}$, where the length of the GIMF section is given by $\tilde{L} = 300\pi + \delta\tilde{L}$. τ presented in this figure is the average value between $\tau|_{\tilde{\gamma}=0.001}$ and $\tau|_{\tilde{\gamma}=0}$. This figure is intended to show that the value of τ is not too low near the peak value of $(\delta\tau/\tau)$ in Fig. 15. The plots are presented for $\eta = 2$ (solid) and $\eta = 3$ (dashed).

15% is possible in this case. While this may seem like a highly desirable SA, the relative power transmission plot for $\eta = 4$ in Fig. 18 shows that τ is quite small near the peak values of $(\delta\tau/\tau)$. Perhaps an optimum operation of this device can be accomplished at $\delta\tilde{L} \approx -0.3$ where $\delta\tau/\tau \approx 9\%$.

5. Discussion and Conclusion

In this paper, a detailed analysis of the NL-MMI behavior of the SMF-GIMF-SMF geometry shown in Fig. 1 has been presented. Recently, this setup was successfully used to create very low-loss couplers between two SMFs with very different mode-field diameters [9,10]. Here, it has been shown that the transmission through this coupler has a very interesting nonlinear behavior and can be potentially used for switching purposes or for saturable

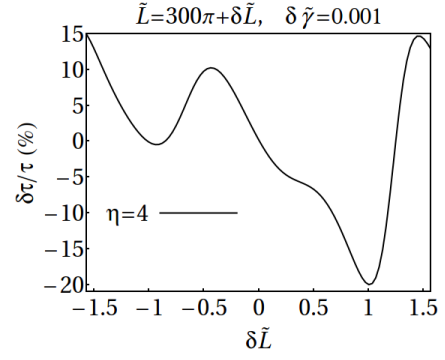


Fig. 17. Same as Fig. 15, except for $\eta = 4$.

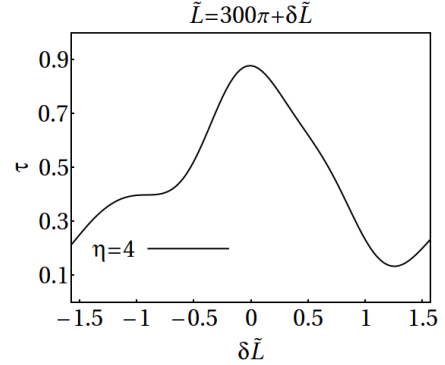


Fig. 18. Same as Fig. 16, except for $\eta = 4$.

absorption in all-fiber mode-locked lasers.

The key parameters that affect the NL-MMI in this geometry are the ratio of the mode-field diameter of the LG₀₀ mode in GIMF to the mode-field diameters of the SMFs (characterized by η defined in Eq. 17); the length of the GIMF section (characterized by the relative length parameter \tilde{L}); the relative nonlinear coefficient $\tilde{\gamma}$, which incorporates the total power and nonlinear coefficient of the GIMF; and the total number of propagating modes in the GIMF.

It was observed that the best performances for switching and intensity discrimination applications such as in SAs can be obtained when the value of η defined in Eq. 17 is not too large; $\eta < 4$ seems like a reasonable choice. This is easily achievable for reasonable selection of commercially available fibers.

Like most other nonlinear devices, the interaction length plays a very important role in the behavior of the SMF-GIMF-SMF device. The dimensionless normalized length \tilde{L} has been used throughout this paper, which is the length of the GIMF normalized by $\beta_{(1)} - \beta_{(2)}$. This normalization factor is $(183 \mu\text{m})^{-1}$ for a C-GIMF operating at 1550 nm. Therefore, $\tilde{L} = 4.5\pi$, $\tilde{L} = 100.5\pi$, and $\tilde{L} = 300\pi$ used in this paper translate to $L=2.6$ mm, 5.78 cm, and 17.24 cm for the length of the GIMF section, which are all reasonable lengths for device applications. For SA purposes, $\tilde{L} = 300\pi + \delta\tilde{L}$ was explored in Figs. 15 and 17, where it was realized that some level of fine-tuning of the order of $\delta\tilde{L} \sim \pi$ is required, which

is $\delta L \sim 575 \mu\text{m}$ for C-GIMF at 1550 nm wavelength. This situation is not different from that of Refs. [9,10], and the fact that the required fine-tuning range is so small means that it can be easily achieved by polishing the GIMF to the desired length. It should be emphasized that the problem of fine-tuning is not very serious and the length needs to be adjusted over a maximum one period of $\delta\tilde{L} \sim \pi$, because reducing \tilde{L} to $\tilde{L} - \pi$ shifts the periodic transmission pattern by one full period. Other pragmatic approaches can be taken instead of fine-tuning the length. For example, an ensemble of twenty SMF-GIMF-SMF couplers can be built around the same average GIMF length; using this approach, the value of $\delta\tilde{L}$ will be uniformly distributed over the range of $[-\pi/2, +\pi/2]$ and one of the elements of the ensemble will likely perform up to the required specification.

The relative nonlinear coefficient $\tilde{\gamma}$ is defined in Eq. 12. For C-GIMF at 1550 nm wavelength, $\tilde{\gamma}=1.0$ corresponds to a power of $\tilde{P} \approx 10.0$ MW, given that the nonlinear coefficient γ (defined for the LG₀₀ mode in GIMF) is smaller than that of the SMF-28 by a factor $\eta \approx 2.2$. For practical fiber-based mode-locking applications, this value is unacceptably large. The feasible range of operation for the peak-power of a mode-locked fiber laser is in the several to a likely maximum of a few hundred KW of peak power. If the GIMF is made from highly nonlinear material, e.g., chalcogenide glass with a nonlinear coefficient of up to 1000 times larger than silica, then $\tilde{\gamma}=1.0$ will correspond to $\tilde{P} \approx 10.0$ KW

The feasibility of using the SMF-GIMF-SMF geometry has been shown for SA applications even for $\tilde{\gamma} = 0.001$ in Fig. 17, which corresponds to $\tilde{P} \approx 10.0$ KW using C-GIMF and SMF-28 commercial fibers at 1550 nm wavelength. Therefore, it is probable that the SMF-GIMF-SMF geometry can be used even with conventional commercially available fibers to mode-lock fiber lasers at the presently achievable power levels. The main advantage of this geometry is that it can be designed to operate at a much higher power level compared with the existing SAs that exploit nonlinear polarization rotation, semiconductors, or carbon nanotubes. Therefore, it might offer a very attractive solution for scaling up the pulse energy and peak power in mode-locked fiber lasers that are currently limited by the existing SA technology.

Throughout this paper, it was observed that having a smaller number of propagating modes in the GIMF is beneficial, especially in the design of an SA. While specific designs need to be carefully analyzed using the formalism laid out in this manuscript, this can be taken as a general guideline and highly multimode GIMFs should be avoided if possible. We do not think that the quality and the telecommunication bandwidth of the GIMF (e.g., due to the centerline defect [28]) has any appreciable effect on the NL-MMI behavior and the SA performance of the SMF-GIMF-SMF geometry.

Finally, we would like to comment on the possibility of exciting nonzero angular momentum modes, which are excluded from our analysis. It is possible to ex-

cite $m = \pm 1$ modes via coupling them to $m = 0$ modes by bending the GIMF. In order for the power exchange to operate efficiently in a resonant fashion, the phase mismatch between the $m = 0$ and $m = \pm 1$ must be compensated for by the bend; e.g, long-period gratings are optimized to provide this phase-matching condition [17]. However, in a GIMF, the $m = 0$ and $m = \pm 1$ modes always belong to different mode groups with a very large mismatch in their propagation constants according to Eq. 4; therefore, a very small bending radius (submillimeter for C-GIMF) is required for efficient phase matching. Therefore, coupling between $m = 0$ and $m = \pm 1$ will not be an efficient process in GIMFs, unless assisted by specialty devices such as long-period gratings [17].

Coupling between between $m = 0$ and $m = \pm 2$ is induced via the random variations in the diameter of the GIMF, caused by manufacturing errors [29], and can even happen within the same mode group with minimal phase matching issue. While this can be minimized by selecting a high quality GIMF, in practice, this should not cause any issues for GIMFs shorter than approximately one meter in length.

It has also been previously shown that fabrication errors due to the misalignment of the fibers can be minimized to the extent where they do not have a noticeable impact on the linear operation of the device [10]; similar robustness is expected in the nonlinear regime of operation.

Acknowledgments

The authors acknowledge support from the Air Force Office of Scientific Research under Grant FA9550-12-1-0329.

References

1. A. Mehta, W. S. Mohammed, and E. G. Johnson, "Multimode interference based fiber optic displacement sensor," *IEEE Photon. Tech. Lett.* **15**, 1129–1131 (2003).
2. W. S. Mohammed, A. Mehta, and E. G. Johnson, "Wavelength tunable fiber lens based on multimode interference," *J. Lightwave Technol.* **22**, 469–477 (2004).
3. W. S. Mohammed, P. W. E. Smith, and X. Gu, "All-fiber multimode interference band-pass filter," *Opt. Lett.* **31**, 2547–2549 (2006).
4. Q. Wang and G. Farrell, "All-fiber multimode-interference-based refractometer sensor: proposal and design," *Opt. Lett.* **31**, 317–319 (2006).
5. Y. O. Yilmaz, A. Mehta, W. S. Mohammed, and E. G. Johnson, "Fiber-optic beam shaper based on multimode interference," *Opt. Lett.* **32** 3170–3172 (2007).
6. X. Zhu, A. Schülzgen, H. Li, L. Li, L. Han, J. V. Moloney, and N. Peyghambarian, "Detailed investigation of self-imaging in large-core multimode optical fibers for application in fiber lasers and amplifiers," *Opt. Express* **16**, 16632–16645 (2008).
7. X. Zhu, A. Schülzgen, L. Li, and N. Peyghambarian, "Generation of controllable nondiffracting beams using

- multimode optical fibers,” *Appl. Phys. Lett.* **94** 201102 (2009).
8. X. Zhu, A. Schülzgen, H. Li, H. Wei, J. V. Moloney, and N. Peyghambarian, “Coherent beam transformation using multimode waveguides,” *Opt. Express* **18**, 7506–7520 (2010).
 9. A. Mafi, P. Hofmann, C. Salvin, and A. Schülzgen, “Low-loss coupling between two single-mode optical fibers with different mode-field diameters using a graded-index multimode optical fiber,” *Opt. Lett.* **36**, 3596–3598 (2011).
 10. P. Hofmann, A. Mafi, C. J. Salvin, T. Tiess, N. Peyghambarian, and A. Schülzgen, “Detailed investigation of mode-field adapters utilizing multimode-interference in graded index fibers,” *J. Lightwave Technol.* **30**, 2289–2297 (2012).
 11. G. P. Agrawal, *Fiber-Optic Communication Systems*, 4th ed. (Wiley, 2011).
 12. M. I. Dzhibladze, Z. G. Esiashvili, E. S. Teplitskii, S. K. Isaev, and V. R. Sagaradze, “Mode-locking in a fiber laser,” *Kvantovaya Elektron.* **10**, 432434 (1983).
 13. L. F. Mollenauer and R. H. Stolen, “The Soliton Laser,” *Opt. Lett.* **9**, 13–15 (1984).
 14. D. Gloge and E. A. J. Marcatili, “Multimode theory of graded-core fibers,” *Bell. Syst. Tech. J.* **52**, 1563–1578 (1973).
 15. K. Okamoto, *Fundamentals of optical waveguides*, 2nd ed. (Academic Press, 2006).
 16. M. Mayeh and F. Farahi, “Laser beam shaping and mode conversion in optical fibers,” *Photonic Sensors* **1**, 187–198 (2011).
 17. M. Sumetsky and S. Ramachandran, “Multiple mode conversion and beam shaping with superimposed long period gratings,” *Opt. Express* **16**, 402–412 (2008).
 18. G. J. Liu, B. M. Liang, Q. Li, and G. L. Jin, “Beam propagation in nonlinear multimode interference waveguide,” *J. Opt. A: Pure Appl. Opt.* **7**, 457–462 (2005).
 19. G. I. Stegeman and E. M. Wright, “All-optical waveguide switching,” *Opt. Quantum Electron.* **22** 95–122 (1990).
 20. H. G. Winful and D. T. Walton, “Passive mode locking through nonlinear coupling in a dual-core fiber laser,” *Opt. Lett.* **17**, 1688–1690 (1992).
 21. J. Proctor and J. N. Kutz, “Nonlinear mode-coupling for passive mode-locking: application of waveguide arrays, dual-core fibers, and/or fiber arrays,” *Opt. Express* **13**, 8933–8950 (2005).
 22. D. N. Christodoulides, F. Lederer, and Y. Silberberg, “Discretizing light behaviour in linear and nonlinear waveguide lattices,” *Nature*. **424** 817–823 (2003).
 23. R. H. Stolen, J. Botineau, and A. Ashkin, “Intensity discrimination of optical pulses with birefringent fibers,” *Opt. Lett.* **7**, 512–514 (1982).
 24. G. P. Agrawal, *Nonlinear Fiber Optics*, 5th ed. (Academic Press, 2012).
 25. A. Mafi, “Pulse propagation in a short nonlinear graded-index multimode optical fiber,” *J. Lightwave Technol.* **30**, 2803–2811 (2012).
 26. A. Chong, J. Buckley, W. Renninger, and F. Wise, “All-normal-dispersion femtosecond fiber laser,” *Opt. Express* **14**, 10095–10100 (2006).
 27. F. Kartner, J. aus der Au, and U. Keller, “Slow and fast saturable absorbers for modelocking of solid state lasers – What’s the difference?,” *IEEE J. Sel. Top. Quantum Electron.* **4**, 159–168 (1998).
 28. A. Mafi, “Bandwidth improvement in multimode optical fibers via scattering from core inclusions,” *J. Lightwave Technol.* **28**, 1547–1555 (2010).
 29. R. Olshansky, “Mode Coupling Effects in Graded-index Optical Fibers,” *Appl. Opt.* **14**, 935–945 (1975).